The Astrophysical Journal, 836:197 (15pp), 2017 February 20 https://doi.org/10.3847/1538-4357/aa5b83

Multi-fluid Modeling of Magnetosonic Wave Propagation in the Solar Chromosphere: Effects of Impact Ionization and Radiative Recombination

Yana G. Maneva[1], Alejandro Alvarez Laguna[1,2], Andrea Lani[2], and Stefaan Poedts[1]
[1] Department of Mathematics, Center for Mathematical Plasma Astrophysics, Catholic University of Leuven, B-3001 Leuven, Belgium; yana.maneva@ws.kuleuven.be, stefaan.poedts@wis.kuleuven.be
[2] von Karman Institute for Fluid Dynamics, CFD group, Aeronautics and Aerospace, Rhode Saint-Genèse, Belgium; alejandro.alvarez.laguna@vki.ac.be, lani@vki.ac.be
Received 2016 July 27; revised 2017 January 18; accepted 2017 January 21; published 2017 February 21

Abstract

In order to study chromospheric magnetosonic wave propagation including, for the first time, the effects of ion–neutral interactions in the partially ionized solar chromosphere, we have developed a new multi-fluid computational model accounting for ionization and recombination reactions in gravitationally stratified magnetized collisional media. The two-fluid model used in our 2D numerical simulations treats neutrals as a separate fluid and considers charged species (electrons and ions) within the resistive MHD approach with Coulomb collisions and anisotropic heat flux determined by Braginskiis transport coefficients. The electromagnetic fields are evolved according to the full Maxwell equations and the solenoidality of the magnetic field is enforced with a hyperbolic divergence-cleaning scheme. The initial density and temperature profiles are similar to VAL III chromospheric model in which dynamical, thermal, and chemical equilibrium are considered to ensure comparison to existing MHD models and avoid artificial numerical heating. In this initial setup we include simple homogeneous flux tube magnetic field configuration and an external photospheric velocity driver to simulate the propagation of MHD waves in the partially ionized reactive chromosphere. In particular, we investigate the loss of chemical equilibrium and the plasma heating related to the steepening of fast magnetosonic wave fronts in the gravitationally stratified medium.

Key words: atomic processes – shock waves – Sun: chromosphere – Sun: magnetic fields – Sun: oscillations

1. Introduction

Neutrals play an important role in the evolution of the weakly ionized solar chromosphere where the number density of neutrals can vastly exceed the number density of protons. Therefore, modeling that studies the effect of neutrals on the ambient plasma properties is an important task for better understanding the observed emission lines and the propagation of disturbances from the photosphere through the chromosphere and transition region into the solar corona. Previous theoretical analysis and recent spectral analysis of raster scans with *IRIS* data, for instance in the Mg II h 2803 Å chromospheric spectral line, commonly show the occurrence of double peaks in the spectroscopic lines, which could be explained only by the presence of neutrals (De Pontieu et al. 2014; Pereira et al. 2015; Martínez-Sykora et al. 2016).

The solar chromosphere and transition region regulate the mass, energy, and momentum transfer from the underlying photosphere and convection zones into the upper atmospheric layer, known as the corona. It is well known that the complexity of the chromosphere is related to its partially ionized plasma, which does not fulfill local thermodynamical equilibrium. Due to chemical reactions such as impact ionization, the hydrogen gas in the chromosphere varies from predominantly neutral to predominantly ionized, which has important consequences on the fluid behavior of the plasma and can significantly affect the magneto-thermodynamics descriptions. As we follow the decreasing plasma density and pressure gradients through the chromosphere, the plasma behavior changes from highly collisional to weakly collisional and the system transitions from gas-pressure dominated to magnetically driven. These observed plasma properties affect the propagation of magnetohydrodynamic waves through the chromospheric layer and influence the deposit of energy and related plasma heating there.

Up to now, the numerical modeling of plasma field properties and wave propagation within the solar chromosphere extensively includes different sets of multi-dimensional MHD simulations (Hansteen et al. 2006, 2007; Fedun et al. 2009, 2011; Martínez-Sykora et al. 2009; Gent et al. 2013) as well as improved MHD models. The latter include partial ionization effects by including an ambipolar diffusion term in the generalized Ohm's law and in the energy equations, as considered by Khomenko & Collados (2012) and Martínez-Sykora et al. (2012, 2015, 2016). Previously, the effects of partial ionization and their consequence on the chromospheric magneto-thermodynamics have been considered by using generalized Ohm's law in extended MHD approach (Cheung & Cameron 2012; Khomenko & Collados 2012; Martínez-Sykora et al. 2015, 2016) or in radiative-MHD models, based on, for example, the Bifrost code (Gudiksen et al. 2011), which combines MHD equations with non-gray and non-LTE radiative transfer and thermal conduction along magnetic field lines (Martínez-Sykora et al. 2012, 2015, 2016; Carlsson et al. 2016). Adding the effects of partial ionization leads to additional chromospheric heating, which unavoidably depends on the geometry of the model chromospheric magnetic field, as the ambipolar diffusion term in the generalized fluid models is proportional to the perpendicular current (Khomenko & Collados 2012). Alternatively, the multi-fluid simulations presented in this paper more rigorously account for partial ionization effects by considering neutrals as a separate species, which relaxes the possible limitations of state-of-the-art improved MHD approximations. Multi-fluid theory is necessary to correctly describe the short spatial and temporal scales associated with the collisions between different species, since such short scales are not

appropriately treated by the single-fluid theory that uses a generalized Ohm's law.

Recently, more attention has being drawn to the consequences of ion–neutral interactions on the propagation of MHD waves throughout the chromosphere (Soler et al. 2015; Shelyag et al. 2016). Analytical calculations have suggested that the dominant presence of neutrals in the chromosphere would lead to an over-damping of the Alfén waves there, which would change their commonly expected energy deposit in the corona (Soler et al. 2015). Nevertheless, there are no rigorous calculations of partial ionization effects on the propagation and damping of Alfvén, fast, and slow magnetosonic waves in a reactive gravitationally stratified collisional media and their interaction with the surrounding plasma. In this respect the present model provides a first attempt to consider such interactions within chemically reactive multi-fluid simulations.

To pursue this goal we have developed two-dimensional two-fluid simulation setups to study the interaction between charged particles and neutrals in a reactive gravitationally stratified collisional media. The model is a variation of the two-fluid approach recently developed by Leake et al. (2012) to study chromospheric reconnection in a reactive media, where the gravitational force has been neglected and only constant temperature and densities have been considered. In this work, we have extended the model by Leake et al. (2012) to include the observed temperature and density stratification. In addition, considering pure hydrogen plasma, we have removed the additional charge exchange terms introduced by Meier & Shumlak (2012), which in the absence of heavy ions, simply translate into elastic collisions (Vranjes & Krstic 2013; Vranjes 2014). Separate mass, momentum, and energy conservation equations are considered for the ions and the neutrals. Furthermore the interaction between the two fluids is determined by the elastic collisions and the chemical reactions (e.g., impact ionization and radiative recombination), which are provided as additional source terms. To initialize the system, we consider an ideal gas equation of state with equal initial temperatures for the electrons, ions, and the neutrals, but different density profiles for the charged and neutral particles species. The initial temperature and density profiles are height-dependent and follow the Vernazza–Avrett–Loeser (hereafter VAL C) atmospheric model (Vernazza et al. 1981) for the solar chromosphere. To avoid unphysical outflows and artificial heating we search for a chemical and collisional equilibrium between the ions and the neutrals, eliminating the initial hydrodynamic pressure imbalances. Next, we considered the ion–neutral interactions in a partially ionized magnetized plasma with an initial magnetic profile, corresponding to a homogeneous magnetic flux tube. The magnetic field profile is not force free and introduces additional pressure gradients in the upper chromosphere. Finally, we include an external velocity driver and simulate the propagation of magnetosonic waves through the photosphere and the chromosphere.

2. Model Description and Simulation Setup

In this section, we describe in details our two-fluid model, where the protons and electrons are described within a single-fluid MHD description neglecting the electron inertia terms. A separate second fluid is used to describe the evolution of neutrals, which interact with the plasma via elastic collisions, impact ionization, and radiative recombination. The numerical schemes, the model equations, and the initial conditions are explained in the subsections below.

2.1. Numerical Schemes and Boundary Conditions

The 2D two-fluid numerical simulations are carried out using a fully coupled multi-fluid/Maxwell solver (Alvarez Laguna et al. 2016), which has been implemented within COOLFluiD. The latter is an open-source platform for high-performance scientific computing[3] featuring advanced computational models/solvers for tackling re-entry aerothermodynamics (Degrez et al. 2009; Lani et al. 2013a; Munafo et al. 2013; Panesi & Lani 2013; Garicano Mena et al. 2015), simulation of experiments in high-enthalpy facilities (Knight et al. 2012; Zhang et al. 2016), ideal magnetohydrodynamics for space weather prediction (Yalim et al. 2011; Lani et al. 2014), radiation transport by means of ray tracing and Monte Carlo (Santos & Lani 2016) algorithms, etc.

The temporal evolution of the multi-fluid equations is based on an implicit second-order three-point backward Euler scheme, while the spatial derivatives are calculated using a state-of-the-art second-order finite volume method for unstructured grids. The algebraic system resulting from a Newton linearization is solved by means of a Generalized Minimal RESidual (GMRES) algorithm complemented by a parallel preconditioner (Additive Schwartz Method), as provided by the PETSc library (Balay et al. 2015). The Maxwell solver is fully relativistic and includes a divergence-cleaning correction (Munz et al. 2000) to ensure that the magnetic field remains divergence-free. The discretization of the convective fluxes are based on a upwind Advection Upstream Splitting Method (AUSM+up scheme) for the multi-fluid equations and on a modified Steger–Warming scheme for the Maxwell counterpart.

For the purpose of studying wave excitation by photospheric drivers we use a subsonic inlet at the lower boundary with prescribed electromagnetic fields and ion and neutral velocities. The value of the temperature at the lower boundary is imposed and the pressure for both plasma and neutrals is extrapolated to ensure zero pressure gradient at the lower boundary. For the side boundaries and at the top we use supersonic outlet with open boundary conditions, which allows the generated perturbation to propagate out of the simulation domain.

2.2. Model Equations

Here, we present the model equations for the two-fluid treatment, with MHD protons and electrons and a separate fluid description for the neutrals. The continuity, momentum, and energy equations for the reactive and resistive viscous plasma and the neutrals are presented below. The change of plasma and neutral mass density is governed by the interplay of ionization and recombination rates:

$$\frac{\partial \rho_i}{\partial t} + \nabla \cdot (\rho_i \boldsymbol{v}_i) = m_i(\Gamma_i^{\rm ion} + \Gamma_i^{\rm rec}) \quad (1)$$

$$\frac{\partial \rho_n}{\partial t} + \nabla \cdot (\rho_n \boldsymbol{v}_n) = m_n(\Gamma_n^{\rm ion} + \Gamma_n^{\rm rec}), \quad (2)$$

where ρ_i and ρ_n are the mass density of protons and neutrals, $\boldsymbol{v}_i$ and $\boldsymbol{v}_n$ are the corresponding velocities, and $\Gamma_{i,n}^{\rm ion}$ and $\Gamma_{i,n}^{\rm rec}$ are the ionization and recombination rates that satisfy $\Gamma_i^{\rm ion} = -\Gamma_n^{\rm ion}$

[3] https://github.com/andrealani/COOLFluiD/wiki

and $\Gamma_i^{\rm rec} = -\Gamma_n^{\rm rec}$. The explicit formulas for the ionization rates and the corresponding cross sections for the chemical reactions are presented below in a subsection devoted to describing the initial chemical equilibrium. The momentum equations for the plasma and the neutral fluids are given by

$$\begin{aligned}\frac{\partial \rho_i \boldsymbol{v}_i}{\partial t} &+ \nabla \cdot (\rho_i \boldsymbol{v}_i \boldsymbol{v}_i + p_i + p_e) \\ &= -\nabla \cdot (\pi_i) + \boldsymbol{j} \times \boldsymbol{B} + \boldsymbol{R}_i^{in} \\ &\quad + \rho_i \boldsymbol{g} + \Gamma_i^{\rm ion} m_i \boldsymbol{v}_n - \Gamma_n^{\rm rec} m_i \boldsymbol{v}_i, \end{aligned} \tag{3}$$

$$\begin{aligned}\frac{\partial \rho_n \boldsymbol{v}_n}{\partial t} + \nabla \cdot (\rho_n \boldsymbol{v}_n \boldsymbol{v}_n + p_n) &= -\nabla \cdot (\pi_n) - \boldsymbol{R}_i^{in} + \rho_n \boldsymbol{g} \\ &\quad - \Gamma_i^{\rm ion} m_i \boldsymbol{v}_n + \Gamma_n^{\rm rec} m_i \boldsymbol{v}_i, \end{aligned} \tag{4}$$

where p_i and p_n are the corresponding pressures for the ions and the neutral fluid, respectively. The first equation describes the momentum transfer of the MHD plasma, including both charged particles (protons and electrons), therefore the gradient of the electron pressure $p_e = p_i$ is included in the plasma flux. In this study the electron inertia terms are neglected. Furthermore, we assume charge neutrality $n_e = n_i$ and equal temperatures between the two charged particles $T_e = T_i$. The stress tensor components for both ions and neutrals follow the standard expression (Leake et al. 2012)

$$\pi_{i,lm} = -\mu_i \left[\left(\frac{\partial v_m^i}{\partial x_l} + \frac{\partial v_l^i}{\partial x_m} \right) - \frac{2}{3} \frac{\partial v_k^i}{\partial x_k} \delta_{lm} \right], \tag{5}$$

where μ is the dynamic viscosity coefficient. For the ions we select $\mu_i = 0.02$ [Pa s] and for the neutrals $\mu_n = 1$ [Pa s]. Currently our model does not include the effect of the perpendicular and the gyro viscosities on ions. The neutrals do not directly feel the magnetic field and they would experience only the parallel viscosity that enters in the current form of the stress tensor. We should note that for the selected VAL C model density and temperature stratification, the collisions between ions and neutrals are very frequent. Simultaneously, the selected magnetic field strength is rather weak at the photosphere and low chromosphere (only 18 G), which leaves the ions unmagnetized in the entire domain until the upper chromosphere above 1.6 Mm, where the magnetic field overcomes the ion–neutral collisional frequencies and the ions become magnetized. In this respect we expect that the effect of the different viscosities would be important only in the upper chromosphere and above (in the transition region, solar corona, and solar wind). We could speculate that if the anisotropic viscosities are taken into account, then we would expect to see some stronger heating in the upper chromosphere. However, it has been previously shown that the viscous stress heating is overcome by the Ohmic heating and the Ambipolar diffusion heating terms (see Khomenko & Collados 2012). In this respect we do not expect the inclusion of anisotropic viscosities to significantly influence our results. We should note that the ion–neutral and electron–neutral collisions significantly overcome the ion–ion and electron–electron collisions within the photosphere up to the upper chromosphere almost at the end of the simulation box. The electron–ion collisions become significant at lower altitudes. Another concern is that in reality the transport coefficients strongly depend on the plasma properties, such as the plasma density and temperature. Still, the height variation of the viscosity is much smoother than the height dependence of the Ambipolar viscosity (Khomenko & Collados 2012). We have discussed the implications of height-dependent viscosity and thermal conduction coefficients for our results in Sections 3 and 3.2.

The current $\boldsymbol{j}$ in the Lorentz force $\boldsymbol{j} \times \boldsymbol{B}$ is given by the generalized Ohm's law presented below and the gravity force in the chromosphere is well approximated by a constant solar acceleration in vertical direction $g = -274.78\ {\rm m\ s^{-2}}$. The elastic collisions between the ions and neutrals are described for example, in (Leake et al. 2012, 2013)

$$\boldsymbol{R}_i^{in} = m_{in} n_i \nu_{in} (\boldsymbol{v}_n - \boldsymbol{v}_i), \quad \nu_{in} = n_n \Sigma_{in} \sqrt{\frac{8 k_B T_{in}}{\pi m_{in}}}, \tag{6}$$

where $m_{in} = \frac{m_i m_n}{m_i + m_n}$ is the center of momentum mass. ν_{in} is the collisional frequency in Hz, which depends on the average temperature $T_{in} = (T_i + T_n)/2$ and the collisional cross section $\Sigma_{in} = \Sigma_{ni}$. Recent estimates, which are based on atomic physics calculations, show that the temperature dependence of the collisional cross sections in the selected chromospheric region is insignificant (Vranjes & Krstic 2013; Vranjes 2014). Therefore, for the purpose of our study we have selected constant cross sections $\Sigma_{ni} = 1.16 \cdot 10^{-18}$ [m^2] as considered in Leake et al. (2013). For the purely electron-hydrogen plasma, which is considered here with no heavy ions, the effect of the charge exchange is reduced to regular elastic collisions (Vranjes & Krstic 2013) and therefore it is not taken into account separately, as done for example in Meier & Shumlak (2012). The momentum transfer due to inelastic collisions is discussed in more details in the next subsection. The corresponding energy conservation laws for the charged and neutral fluids follow the equations

$$\begin{aligned}\frac{\partial}{\partial t}\left(\varepsilon_i + \frac{\gamma_e p_e}{\gamma_e - 1}\right) &+ \nabla \cdot \left(\varepsilon_i \boldsymbol{v}_i + \frac{p_e}{\gamma_e - 1} \boldsymbol{v}_i + p_i \boldsymbol{v}_i\right) \\ &= -\nabla \cdot (\boldsymbol{v}_i \cdot \pi_i + \boldsymbol{q}_i + \boldsymbol{q}_e) + \boldsymbol{j} \cdot \boldsymbol{E} \\ &\quad + \boldsymbol{v}_i \boldsymbol{R}_i^{in} + \rho_i \boldsymbol{v}_i \cdot \boldsymbol{g} \quad + Q_i^{in} - \Gamma_n^{\rm rec} \frac{1}{2} m_i v_i^2 \\ &\quad - Q_n^{\rm rec} + \Gamma_i^{\rm ion} \left(\frac{1}{2} m_i v_n^2 - \phi_{\rm ion}\right) + Q_i^{\rm ion}, \end{aligned} \tag{7}$$

$$\begin{aligned}\frac{\partial \varepsilon_n}{\partial t} &+ \nabla \cdot (\varepsilon_n \boldsymbol{v}_n + \boldsymbol{v}_n p_n) = -\nabla \cdot (\boldsymbol{v}_n \cdot \pi_n + \boldsymbol{q}_n) - \boldsymbol{v}_n \boldsymbol{R}_i^{in} \\ &\quad + \rho_n \boldsymbol{v}_n \cdot \boldsymbol{g} + Q_n^{in} + \Gamma_n^{\rm rec} \frac{1}{2} m_i v_i^2 \\ &\quad + Q_n^{\rm rec} - \Gamma_i^{\rm ion} \frac{1}{2} m_i v_n^2 - Q_i^{\rm ion}, \end{aligned} \tag{8}$$

where, in Equation (7), electrons are considered to move at the ion speed $\boldsymbol{v}_e = \boldsymbol{v}_i$. For the momentum and energy evolution, an ideal gas equation of state is assumed with $p_{i,n} = n_{i,n} k_{\rm B} T_{i,n}$. The adiabatic index for all species is considered equal $\gamma_e = \gamma_i = \gamma_n = 5/3$. The kinetic and internal energies for the protons and neutrals are given by $\varepsilon_{i,n} = n_{i,n}\left(\frac{m_{i,n} v_{i,n}^2}{2} + \frac{k_{\rm B}}{\gamma_{i,n} - 1} T_{i,n}\right)$. The plasma heat flux vector includes contributions from both

electrons and protons and takes into account conductivities parallel and perpendicular with respect to the direction of the external magnetic field (Braginskii 1965). Assuming equal number density and temperature for the ions and electrons, the plasma heat flux becomes (Leake et al. 2012)

$$\boldsymbol{q}^i + \boldsymbol{q}^e = -\kappa_{\parallel}^p \boldsymbol{bb}\nabla T_i - \kappa_{\perp}^p (\mathbb{I} - \boldsymbol{bb})\nabla T_i, \tag{9}$$

where the $\boldsymbol{b}$ is the unit vector in the direction of the magnetic field. The parallel and perpendicular heat conductivities $\kappa_{\parallel}^p$ and $\kappa_{\perp}^p$ for the plasma species "p" are calculated based on the classical transport theory (Braginskii 1965),

$$\kappa_{\parallel}^p = \kappa_{\parallel}^e + \kappa_{\parallel}^i = \left(3.906\frac{\tau_i}{m_i} + 3.1616\frac{\tau_e}{m_e}\right) n_i T_i \tag{10}$$

$$\kappa_{\perp}^p = \kappa_{\perp}^e + \kappa_{\perp}^i = \left[\left(\frac{2(\tau_i\omega_i)_i^2 + 2.645}{\Delta_i}\right)\frac{\tau_i}{m_i} + \left(\frac{4.664(\tau_e\omega_e)_e^2 + 11.92}{\Delta_e}\frac{\tau_e}{m_e}\right)\right] n_i T_i, \tag{11}$$

where τ_e and τ_i accordingly are the temperature and density-dependent collisional times for electrons and protons, $\omega_{e,i}$, and the corresponding cyclotron frequencies, and $\Delta_{i,e} = \tau_{i,e}\omega_{i,e}^4 + 14.79\tau_{i,e}\omega_{i,e}^2 + 3.7703$. The heat conduction for the neutral gas is unaffected by the magnetic field:

$$\boldsymbol{q}_n = -\kappa_n \nabla T_n, \tag{12}$$

where the isotropic heat conductance coefficient is set to $\kappa_n = 0.2$ [W/(m K)] as considered in Leake et al. (2012). We should note that, similar to the viscosity coefficients, the thermal heat conductance also depends on the local plasma parameters, such as density and temperature. Yet, similar to the viscosity, the neutral heat conductivity plays less important of a role than the dominant electron–neutral and the ion–neutral collisions. Although the neutral viscosity and heat conductivity are much higher than the ion ones in the photosphere, low and middle chromosphere their effect is still much less significant in comparison to the effects of the electron–neutral and the ion–neutral collisions. More discussions regarding this are presented in Sections 3 and 3.2.

The electromagnetic fields that enter the momentum and the energy conservation laws are self-consistently evolved according to the full Maxwell equations, which are complemented with the divergence-cleaning electric Φ and magnetic field Ψ potentials. The full Maxwell solver allows for propagation of high-frequency waves, which are neglected by the standard MHD approximation. The hyperbolic divergence-cleaning procedure guarantees that the magnetic field remains divergence-free. Any deviations are instantaneously propagated out with the corresponding characteristic velocities $c\xi$ and $c\gamma$, where c is the speed of light and ξ and γ are positive parameters as described in Munz et al. (2000) and Alvarez Laguna et al. (2016):

$$\frac{\partial \boldsymbol{B}}{\partial t} + \nabla \times \boldsymbol{E} + \gamma\nabla\Psi = 0 \tag{13}$$

$$\frac{\partial \boldsymbol{E}}{\partial t} - c^2\nabla \times \boldsymbol{B} + \xi c^2 \nabla\Phi = -\frac{\boldsymbol{j}}{\epsilon_0} \tag{14}$$

$$\nabla \cdot \boldsymbol{B} = 0 \tag{15}$$

$$\nabla \cdot \boldsymbol{E} = \frac{\rho_c}{\epsilon_0}. \tag{16}$$

In order to compare our results to existing MHD simulations of chromospheric wave propagation, in this study, the current is computed by a simplified version of the generalized Ohm's law, where we neglect the secondary effects of electron inertia $\frac{m_e}{n_e e^2}\frac{d\boldsymbol{j}}{t}$, the Hall term $\frac{\boldsymbol{j}\times\boldsymbol{B}}{en_e}$, the battery term $\frac{1}{en_e}\nabla\cdot\mathbb{P}_e$ related to the divergence of the electron pressure tensor $\mathbb{P}_e$, and the electron–neutral collisions $\frac{m_e\nu_{en}}{e}(\boldsymbol{v}_i - \boldsymbol{v}_n)$. Under these assumptions the resistive Ohm's law takes the simplified form

$$\boldsymbol{E} + \boldsymbol{v}_i \times \boldsymbol{B} = \eta \boldsymbol{j}. \tag{17}$$

To compute the electrical resistivity, η, we calculate both the collisional frequencies of electrons with ions and electrons with neutrals, $\eta = m_e n_e(\nu_{en} + \nu_{ei})/(e^2 n_e^2)$, following the expressions (Braginskii 1965; Soler et al. 2015)

$$\nu_{en} = n_n \Sigma_{en}\sqrt{8k_B T_{en}/(\pi m_{en})} \tag{18}$$

$$\nu_{ei} = n_i \Sigma_{ei}\sqrt{8k_B T_{ei}/(\pi m_{ei})}, \tag{19}$$

where $m_{ei} = m_e m_i/(m_e + m_i)$ is the center of mass between electrons and ions, and $T_{ei} = T_i$, $T_{en} = T_{in}$ are the average temperatures. The collisional cross section between ions and electrons is computed from Braginskii's expressions (Braginskii 1965), $\Sigma_{ei} = \lambda_C \pi \lambda_D^2$, where $\lambda_D = e^2/(4\pi\epsilon_0 k_B T_i)$ is the Debye length and $\lambda_C = 10$ is the approximate value of the Coloumb logarithm in the chromosphere. The collisional cross section for electron–neutral collisions is taken to be $\Sigma_{en} = 10^{-18}$ [m^2], although quantitatively similar results are obtained when a smaller collisional cross section is used with $\Sigma_{en} = 3\cdot 10^{-19}$ [m^2]. The conductivity is inversely proportional to the electrical resistivity $\sigma = \eta^{-1}$.

2.3. Initial Conditions: Thermal and Chemical Equilibrium

In order to model the reactive inhomogeneous chromospheric plasma, we initialize the code with a height-dependent temperature profile, given by the original VAL C chromospheric model (Vernazza et al. 1981). The VAL C model, as well as the more recent follow-up chromospheric models (Fontenla et al. 1993), do not distinguish between the temperature of molecular hydrogen and protons and provide a single temperature profile for the single ionized hydrogen and the neutrals. The lack of observational data for the separate temperature profiles of neutrals and ions poses a problem for a realistic non-LTE multi-fluid modeling. Therefore, to best relate to the existing global atmospheric models within our two-fluid description we have assumed an initially isothermal plasma with $T_e = T_i = T_n$. The initial density profiles for the neutrals has also been adopted from VAL C model (Vernazza et al. 1981). The initial proton density follows a modified VAL C profile, which assumes initial chemical equilibrium. Given the fact that our model is based on initially isothermal single ionized proton–electron plasma with neutral hydrogen and currently does not take into account chemical reactions that involve heavier species, adopting the VAL C atmospheric density profiles for the protons and neutrals results in a chemical imbalance between the ionization and the recombination rates. This imbalance could be resolved if different

temperature profiles for the protons and neutrals are assumed. However, such different temperature profiles are currently not provided by observations and including them would make the comparison to existing (generalized) MHD models more difficult. The ionization and the recombination coefficients in $[m^3\,s^{-1}]$ for hydrogen plasma used in our study follow the expressions in (Cox & Tucker 1969; Moore & Fung 1972)

$$I = 2.34 \cdot 10^{-14}(\sqrt{\beta}\exp(-\beta)) \quad (20)$$

$$R = 5.20 \cdot 10^{-20}\sqrt{\beta}(0.4288 + 0.5\log\beta + 0.4698\beta^{-1/3}), \quad (21)$$

where $\beta = A \cdot \Phi_{\rm ion}/T_e^{\star}$ is a dimensionless parameter that takes into account the temperature dependence of the ionization and recombination rates. In this expression, $T_e^{\star}$ is the electron temperature in eV, $\Phi_{\rm ion} = 13.6$ eV is the ionization potential for hydrogen atoms, and $A = 0.6$ is a constant, which takes into account the influence of heavy ions and has been introduced to match the expected ionization rates n_i/n_n, as predicted by the VAL C model (Vernazza et al. 1981). We should note that despite the different functional form for the selected temperature range, these ionization and recombination coefficients are practically identical to the ones proposed by Voronov (1997) and Smirnov (2003), which have been used in the multi-fluid modeling by Leake et al. (2012). The ionization and recombination rates that account for the mass, momentum, and energy transfer in the multi-fluid system read

$$\Gamma_i^{\rm ion} = n_n n_i I, \quad \Gamma_n^{\rm rec} = n_i^2 R. \quad (22)$$

In order to build a solid physical understanding of the reactive multi-fluid problem and for the sake of comparison to results from existing fluid theories, we have initialized the code assuming a chemical equilibrium, where the ionization and the recombination rates initially balance each other $\Gamma_i^{\rm ion} = \Gamma_n^{\rm rec}$. Therefore, if we assume an initially isothermal plasma with temperature and neutral density profiles following the tabulated values from VAL C model (Vernazza et al. 1981), in order to maintain a chemical equilibrium for the neutrals we need to slightly modify the ion density profile. Figure 1 represents a 1D cut with the initial mass density and temperature profiles used in the simulations. All plasma parameters vary with the heliocentric distance and the neutral density changes by five orders of magnitude. The ions and neutrals are initially considered in thermal equilibrium with $T_i = T_n$. The modified plasma density in our model has similar shape to the inferred electron density presented in the chromospheric model by Avrett & Loeser (2008). The initial profiles capture the photospheric temperature minimum around 500 km and the consequent temperature increase in the upper chromosphere. The ionization level increases as the neutral and ion densities become more comparable in the upper chromosphere. The 2D contour plots of the initial temperature profile and its variation throughout the simulations are presented in the Results section in Figure 3.

In the next section we present in details the results from the simulations and discuss their relation to previous models in the available literature.

3. Numerical Results

In this section, we will present the main results of our numerical study on chromospheric wave propagation. The multi-fluid simulations are performed based on dimensional quantities and all results are provided in SI units. Where necessary, an appropriate conversion from CGS or other units has been introduced to correct for the different expressions of the source terms and the transport coefficients as provided in the literature. For visualization purposes, we use a Cartesian grid where the heliocentric distance is represented by the vertical y axis and the horizontal variations are given in x direction. The physical size of the box is 2 Mm by 2 Mm and we have used a moderate spatial resolution of 200 grid points in each direction. We should note that increasing the resolution does not significantly affect the wave propagation, but increases the initial force imbalance due to sharper gradients and results in stronger velocity outflows.

The first subsection describes the initial magnetic field configuration and the applied photospheric velocity driver. The second subsection describes the wave propagation, properties, plasma energetics, and temperature changes for different driver periods.

3.1. Magnetic Field Configuration and Photospheric Velocity Driver

In order to study the evolution of sound and magnetosonic waves in the chromosphere in all cases considered here we have adopted a simple Gaussian magnetic field profile and a photospheric footpoint velocity driver used in MHD and improved partially ionized MHD models with ambipolar diffusion terms, as presented, for example, in (Khomenko et al. 2008; Fedun et al. 2009, 2011)

$$B_y(x) = B_0\exp\left(-\frac{(x-x_0)^2}{2\sigma^2}\right), \quad (23)$$

$$V_{x,y}(x,t) = V_0\sin(2\pi\nu t)\exp\left(-\frac{(x-x_0)^2}{2\sigma^2}\right). \quad (24)$$

As a first approximation, the magnetic field strength has been set to $B_0 = 18$ G and we have neglected the initial height dependence of the magnetic field amplitude. As we shall see later, such a height dependence self-consistently develops in the solution in the course of evolution. The initial flux tube is placed in the center of the domain at $x_0 = 1$ Mm and the width of the initial magnetic field footpoint has been selected to $\sigma = 40$ km as in Khomenko & Collados (2012). The magnitude of the velocity driver is set to 500 m s^{-1} as assumed in Fedun et al. (2009). The period of the driver was set to 100, 30, 10, and 3 s with corresponding driver frequencies of $\omega = 2\pi\nu = 0.06$, 0.2, 0.6, and 2.1 Hz. From the various driver frequencies in the results below we will focus on the cases of 30 and 10 s periods. The time step used for the simulations gradually varies throughout the evolution between 10^{-4} and 10^{-2} s. The results form these different cases are presented in the next subsection. We note that the selected initial magnetic field profile is divergence-free, but not force-free and it does carry some current. Due to the low magnitude of the magnetic field considered here, the Lorentz force associated with it is rather small, i.e., on the order of 10^{-5} N. Nevertheless, this force becomes significant in the upper chromosphere, where the pressure gradient and the gravity are substantially reduced due to the depleted plasma density in this region. These currents cause plasma expansion due to the current-related

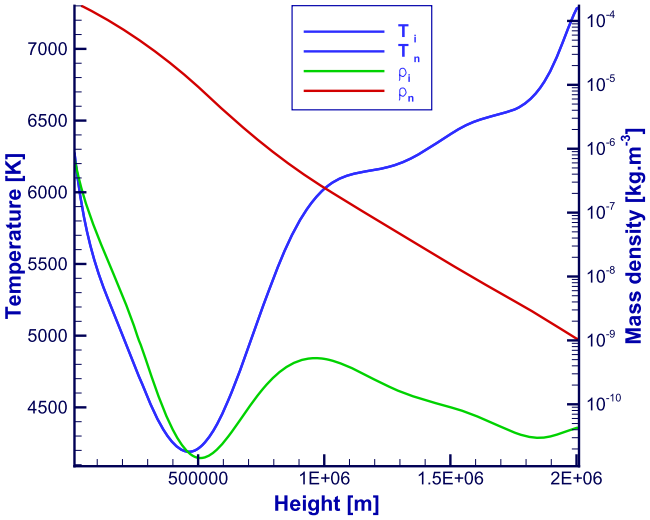

Figure 1. Initial temperature and density profiles, based on a modified VAL C atmospheric model in thermal and chemical equilibrium.

horizontal outflows in the upper chromosphere, resulting in plasma cooling, as described later in this paper.

To compare our results to previous MHD and generalized MHD simulations we used several different initial simulation setups. In order to generate acoustic and magnetosonic waves in the photosphere, we perturbed the horizontal and vertical velocities of the ions, as well as the horizontal and vertical velocities of the neutrals. The main difference between applying the velocity driver on the ions and the neutrals is in the amplitude of the excited perturbations. Since ions are much less abundant than neutrals, while perturbing the ion velocity we input less kinetic energy into the system: this generates smaller pressure gradients and results in less intense waves. However, apart from their amplitude, all physical quantities (e.g., wave properties, velocity, and temperatures profiles) remain practically the same. The small velocity difference between ions and neutrals comes from the Lorentz force, which acts only on the ions. However, the ion–neutral collisions are so frequent, that they efficiently reduce the velocity differences and induce strong coupling between the two species throughout the chromosphere. For a better representation, in the remainder of the paper we will concentrate on the case of velocity driver applied on the neutrals. Figure 2 describes the initial magnetic field and the evolved profiles at a later stage. The background magnetic field evolves in a similar manner for the driven simulations with the various driver's periods considered in our study. Here, we have chosen to plot the evolution of the vertical magnetic field component for case of driver with 30 s (middle) and 10 s (right) periods as an example. The initial magnetic field is given on the left panel and has a Gaussian profile, following Equation (23). It has a maximum magnitude of 18 G inside the flux tube and zero value outside the tube. The middle and right-hand panels describe the evolution of the magnetic field at a later stage at $t = 458$ s. The evolved states show strong diffusion of the magnetic field at the location of the temperature minimum in the photosphere. Since the resistivity in our study is defined within the classical transport theory (Braginskii 1965; Spitzer 1956), it has a strong dependence on the temperature $\eta \propto T^{-3/2}$. The initial density profile for the ions also enhances the resistivity in the photosphere close to the temperature minimum. Therefore, the observed diffusion of the magnetic field is related to resistive dissipation and occurs in the region where the resistivity is strongest. The magnetic field diffusion in the upper part of the chromosphere is related to Ohmic dissipation in the region where the Lorentz force becomes comparable to the otherwise dominant pressure gradient. The lower chromosphere is dominated by the pressure gradients, gravity, and collisions. In the upper chromosphere, the current associated with the initial magnetic field profile leads to strong horizontal flows (with maximum velocities of the order of 1–2 km s^{-1}), which result in expansion of the flux tube. Toward the end of the simulations the flux tube opens up and starts to resemble the observed magnetic funnels. These effects are preserved when a temperature- and density-dependent viscosity model is considered.

3.2. Magnetosonic Wave Propagation and Plasma Properties

In this section we will follow the wave propagation excited by a footpoint photospheric driver applied to the vertical velocity of the neutrals and study the related plasma properties.

3.2.1. Heating, Cooling, and Density Depletion

As mentioned above, in the upper chromosphere at $y > 1.6$ Mm the expansion caused by the horizontal flows and the horizontal currents leads to the associated cooling and density depletion of the plasma inside the flux tube. As the plasma cools, it becomes heavy. Inside the flux tube there is no current to push the plasma outwards and the matter starts to fall back toward the lower chromosphere. This leads to an extended region with decreased plasma temperature and depleted density inside the flux tube. Figure 3 illustrates the initial vertical temperature profile (left panel) with homogeneous horizontal distribution and the onset of inhomogeneous horizontal profile (middle and right panels), due to the described expansion and related plasma cooling inside the magnetic flux tube. The middle panel corresponds to a period of 30 s. The right panel shows the temperature variations excited by a photospheric velocity driver with a period of 10 s. Both drivers have been applied to the vertical velocity of the neutrals and result in a similar highly inhomogeneous vertical and horizontal heating at the wave fronts. At $t = 458$ s the velocity drivers have already generated magnetosonic waves and we observe symmetric oscillations in all physical quantities characteristic for the sound and fast magnetoacoustic waves. The vertical driver mixes the cooler plasma from the photosphere with the hotter regions in the mid and upper chromosphere, forming clear wave patterns. Although supersonic shock waves are never formed within our study, super-Alfvénic shocks are formed and as the waves propagate upward some compressional heating at the wave fronts is observed. Within the flux tube the compressional heating is overcome by the cooling caused by the expansion and the plasma there remains cooler. Some additional cooling is also observed near the temperature minimum in the photosphere where the magnetic field diffuses due to the enhanced resistivity, making this layer more unstable. We note that the cooling in the middle of the flux tube is an MHD effect and does not exist in pure hydrodynamic description, as proven by analogous test simulations performed without a magnetic field. As we explained above, the Lorentz force at the upper chromosphere becomes dominant over the gravity and pressure gradient and the associated current results

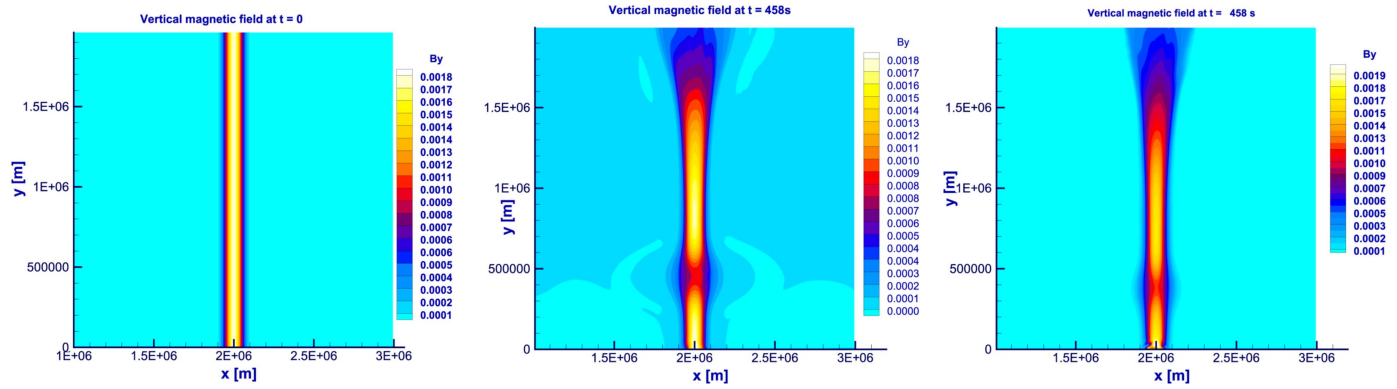

Figure 2. Initial magnetic field profile for the simulations (left) and its evolution at $t = 458$ s for different driver frequencies. The middle panel corresponds to a velocity driver with a period of 30 s, and the right panel corresponds to a driver with a shorter period of 10 s.

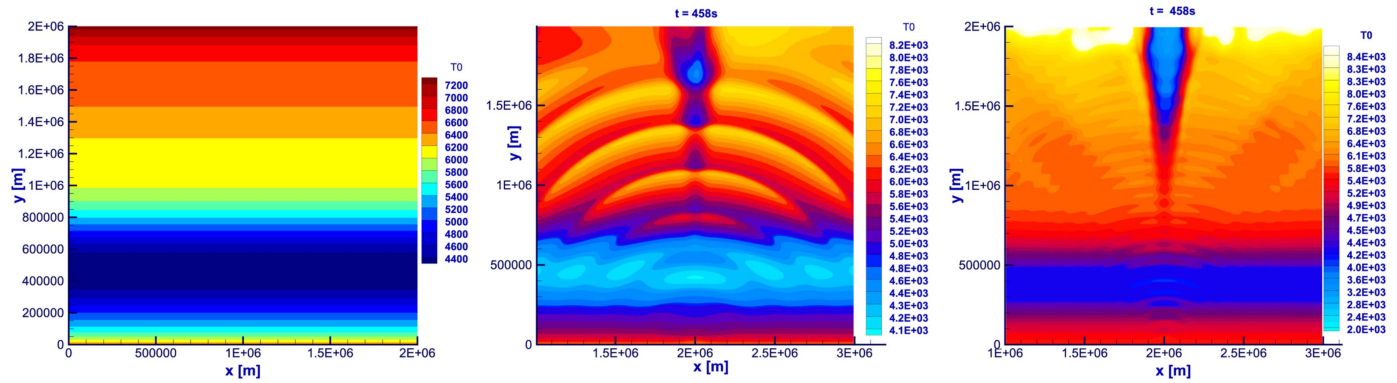

Figure 3. Two-dimensional contour plot with the initial temperature profile (left) and its evolution at $t = 458$ s. The middle panel corresponds to driver's period of 30 s and the right panel stands for a period of 10 s.

in horizontal outflows, causing expansion and resulting in the related cooling of the confined plasma inside the magnetic flux tube. Performing reactive hydrodynamic multi-fluid simulations with exactly the same plasma conditions except for the electromagnetic fields shows no cooling in the upper chromosphere and no significant change in temperature overall, apart from some cooling at the photospheric level close to the initial temperature minimum.

We should note that in extremely dense photospheric and chromospheric conditions the collisional frequency between ions and neutrals is very high and, as discussed above, for pure hydrogen plasma it is comparable to the charge exchange reactions, which in this case can be viewed as part of the elastic collisions (Vranjes & Krstic 2013; Vranjes 2014). As a result, the collisional time is much shorter than the rest of the dynamical timescales in the system throughout the entire photosphere and most of the chromosphere with the exception of the uppermost chromospheric layer. The high collisionality quickly balances out the velocity and temperature differences between the ions and the neutrals, leading to almost single fluid dynamics for the evolution of their fluid velocities and temperature. In this respect, the effect of the electromagnetic fields on the electrons and ions is transported to the neutrals through frequent collisions, so that their temperatures and velocities become practically the same; vice versa, the motion of the neutrals almost simultaneously induces ion motion. Therefore, in the figures below and throughout the paper we show single plots referring to the temperatures and velocities for both species.

Figure 4 shows the observed plasma cooling and the density depletion for both ions and neutrals at the top of the chromosphere, $y = 2$ Mm. The selected driver period for this case is 10 s. The figure shows the initial constant values of the densities and temperature (the constant straight lines) and their depletion and decrease inside the flux tube in the course of evolution. As expected, the minimum of the densities and the temperature is in the center of the flux tube. We should note that although originally only the ions were affected by the horizontal currents, due to the strong collisionality the neutrals follow the ions and their density and temperatures are also reduced. The ion and the neutral densities decrease up to one order of magnitude inside the flux tube and their value outside the flux tube oscillates in time with the propagation of the magnetosonic waves. Within 178 s, the temperature and the densities outside the flux tube are higher than the initial values and the temperature inside the tube is reduced by 2,000 K, from 7400 K to as low as 4700 K. The figure shows the temperature and density profiles within the first six wave periods, before the waves reach the upper boundary. Afterwards, the sound and the fast waves result in density and temperature oscillations with the combination of additional heating/cooling and higher amplitude density fluctuations outside the flux tube. Regardless of the waves, the cooling and density depletion inside the flux tube remain until the end of the simulations and are also present in simulations without

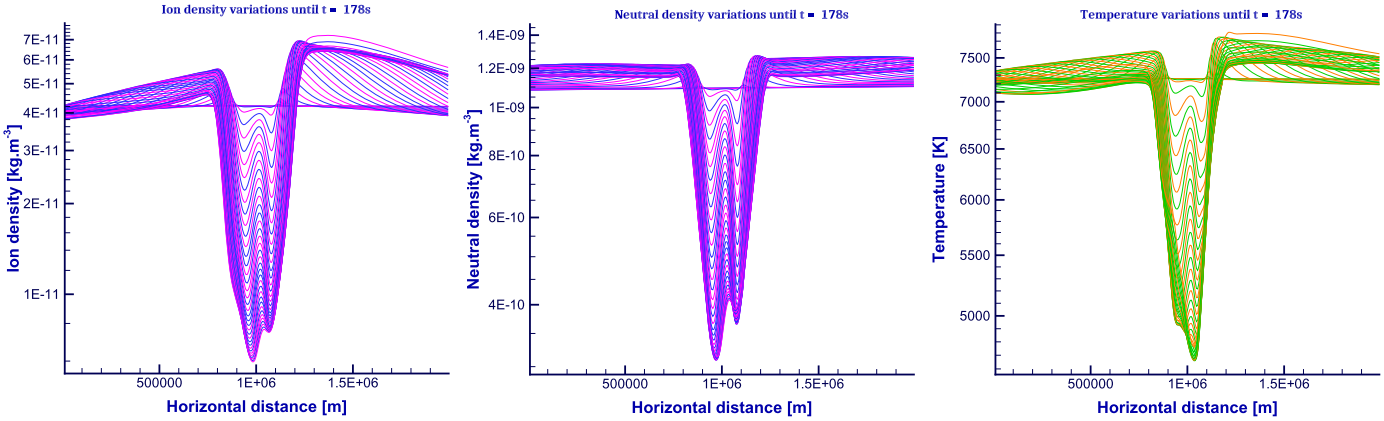

Figure 4. Horizontal variation of the ion (left) and neutral (middle) mass density at the top boundary in time. The right panel describes the corresponding variations of the temperature within the first 178 s.

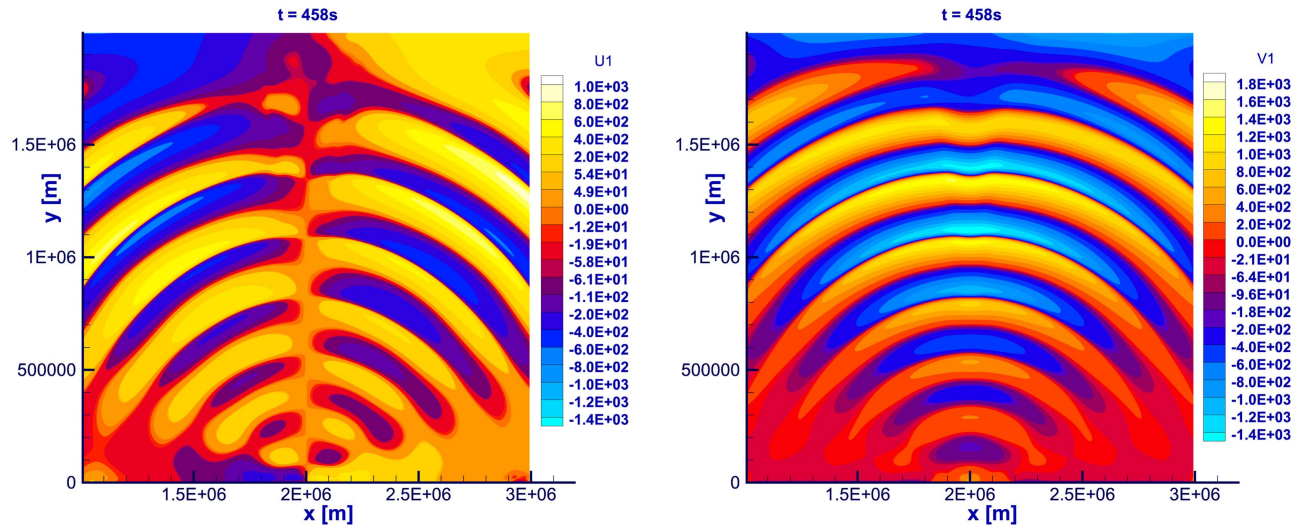

Figure 5. Two-dimensional contour plots with the horizontal (left) and vertical (right) velocity fluctuations at $t = 458$ s. The height dependence is represented in the vertical direction and the longitudinal dependence is given along the horizontal.

an initial driver. We note that the heating at the boundary of the flux tube might be related to ion–neutral interactions as modeled by generalized MHD models, where the heating due to the ambipolar diffusion term is proportional to the perpendicular current. Such scenarios are discussed, for example, by Khomenko & Collados (2012) and Khomenko et al. (2014).

We note here that we have also tested the case of temperature- and density-dependent heat conductivity for the neutrals, as well as ion and neutral viscosities. We observed some slight changes in the temperature in the upper chromosphere, but the overall results for the wave propagation as well as the cooling and density depletion inside the flux tube remained unaffected. Thus, the height-dependent heat conductivity was not able to counter balance the observed cooling inside the flux tube in the upper chromosphere where its effect should be greatest. We should note that having temperature-dependent transport coefficients could facilitate the possible onset of wave conversions at the upper chromosphere. Such processes are out of the main focus of our current study.

3.2.2. Wave Speeds, Plasma Velocities, and Energetics

All results in this subsection concern footpoint drivers applied to the neutrals with a period of 30 s.

Figure 5 shows an example of the horizontal and vertical velocity profiles at $t = 458$ s. This moment in time is not unique and has been randomly selected to illustrate the wave behavior as visible in the two velocity components. Both horizontal and vertical velocity components show symmetric contours typical for sound waves and fast magnetosonic waves propagating along the magnetic field lines. The vertical velocity component is higher than the horizontal velocity. We can also see the change in the plasma velocity related to the distortion of the wave fronts along the flux tube, which becomes clearly visible in the upper chromosphere as we approach the Alfvénic point where $\beta = 1$. In the upper chromosphere, the wave propagation is strongly affected by the magnetic field and we observe a transition from fast to slow magnetosonic waves.

We note that in both magnetized and hydrodynamic multi-fluid cases the initial VAL C atmosphere is slightly convectionally unstable and results in horizontal and vertical flows. One of the reasons for this is that the local thermodynamical equilibrium assumption in their atmospheric model is not fully satisfied. An additional reason is the fixed viscosity coefficients used in our model, which resulted in an under-viscous plasma in the photosphere. Within a physical time of 700 s in both hydro and magnetized cases without an initial wave driver, the maximum velocity amplitude is on the order

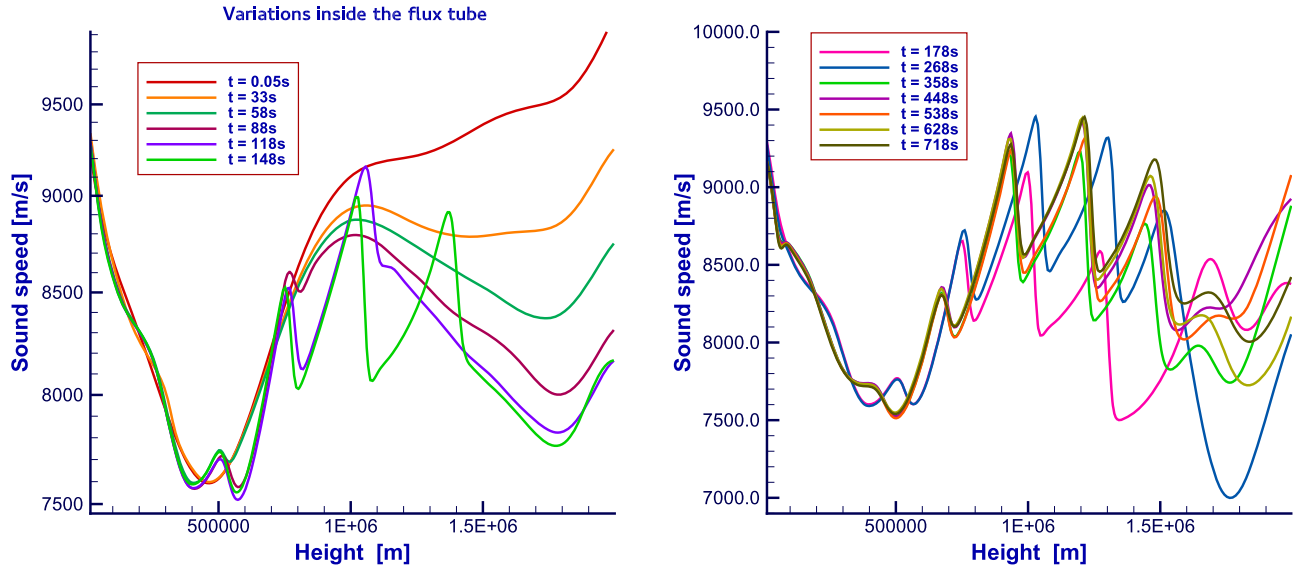

Figure 6. Altitudinal variation of the sounds speed with the wave periods of the initial driver. The vertical cut is taken in the center of the magnetic flux tube. The sound wave speed significantly changes in time and their period varies in the upper chromosphere.

of 1–1.5 km s^{-1} for the horizontal flows and 2–2.5 km s^{-1} for the vertical flows. Typically, the horizontal flows are within 300–500 m s^{-1}. Due to the induced horizontal currents, the applied initial magnetic field profile enhances the horizontal flows in the upper chromosphere where the Lorentz force dominates over the plasma and neutral gas pressure gradients and the plasma β becomes close to unity. Still, without an initial driver the unstable convective flows are at least an order of magnitude smaller than the estimated sound speed throughout the photosphere and chromosphere, as well as the Alfvén, slow (tube), and fast speeds (calculated based upon the total ion and neutral density) inside the magnetic flux tube.

Figure 6 shows the vertical profile of the sound speed $c_s = \sqrt{(\gamma k_B T/m)}$ and its variation in time in the center of the flux tube. The different times have been selected to qualitatively represent the sound speed variations as a function of the initial velocity driver, whose period was set to 30 s. Within the first four wave periods the sound speed decreases in the upper chromosphere, mainly due to the cooling and density depletion caused by the horizontal currents. Within six wave periods the sounds speed starts to oscillate with the amplitude of the driver throughout the entire chromosphere. As the driven waves reach the $\beta = 1$ region in the upper chromosphere, above 1.7 Mm the period of the sound waves oscillations changes due to mode conversion. In addition, the density variations in the upper chromosphere increase as the waves reach the upper boundary, which results in higher amplitude sound waves at $t > 200$ s.

Figure 7 illustrates the temporal evolution of the Alfvén speed in the center of the magnetic flux tube based on the total plasma and neutral density, $V_A = \sqrt{(B/\mu_0 \rho)}$, where $\rho = n_i m_i + n_n m_n$ is the total density. At $t = 0$ the Aflvén speed profile is fully determined by the initial magnetic field and density profiles. As the magnetosonic waves excited by the initial photospheric velocity driver propagate up in the chromosphere, they induce density variations that result in variations of the Alfvén speed over time. Additionally, the magnetic field diffuses both in the photosphere where the *Spitzer* resistivity is highest and in the upper chromosphere, where the cross section of the flux tube increases as the initial vertical flux tube starts to open into a magnetic funnel. This opening leads to diffusion of the magnetic field and results in reduction of the Alfvén speed over time. We note that the deliberate choice of plotting the Alfvén speed based on the total density is made in order to compare the model results and expectations to existing MHD and generalized MHD theories, where the effect of the neutrals is treated as additional terms in the energy and momentum equations of the plasma, but the neutral density is not evolved separately and the plasma density is governed by the charged particles, protons and electrons. As expected due to the huge number density difference between the ions and neutrals, the Alfvén speed based on the ion density inside the flux tube is much bigger and compared to it the plasma flows remain practically sub-Alfvénic at all times in the entire simulation box. Apart from the sound and the Alfvén speed we can also calculate the velocity of the slow magnetosonic waves or the so-called tube speed. Due to the high plasma density in the photosphere and the low chromosphere, the tube speed calculated in the middle of the magnetic flux tube at the lower boundary is only 130 m s^{-1}. Similar to the Alfvén speed, it increases with height and at the top of the chromosphere it becomes more than 40 km s^{-1} and becomes comparable to the sound speed. While the sound speed inside the flux tube decreases in time due to the observed cooling, the tube speed based on the total density gradually increases in height at all times. The tube speed based on the ion density remains quasi conserved throughout the magnetic flux tube with a magnitude of approximately 40 km s^{-1} throughout the chromosphere.

Figure 8 shows the ratio of the Alfvén speed divided by the sound speed, which corresponds to the inverse square root of the plasma β in the center of the magnetic flux tube. The left panel shows the ratio when the magnitude of the Alfvén speed is calculated based on the total density including the contribution of the plasma and the neutrals. The right panel shows the variation of the V_A/c_s ratio when the Alfvén speed is calculated based solely on the plasma density. Clearly, if we consider only the density of the magnetized plasma, the entire chromosphere as well as most of the photosphere would be in a very low plasma β regime, as $\beta \propto c_s^2/V_A$. On one hand, the

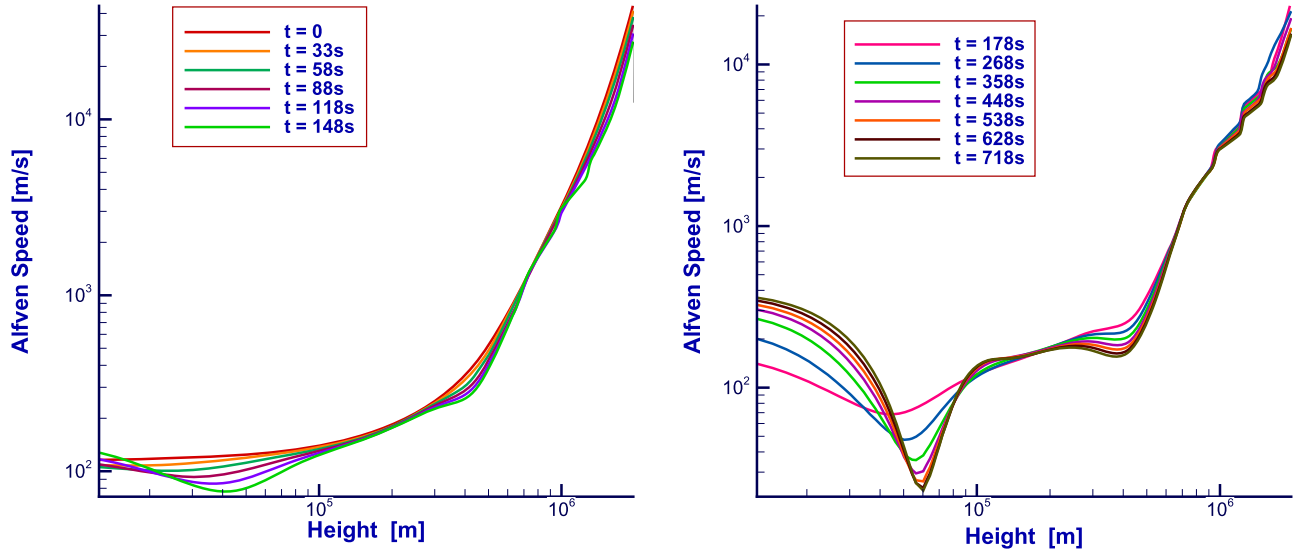

Figure 7. Altitudinal variation of the total Alfvén speed computed based on the total ion and neutral mass density at different times. The plot also shows the temporal variation of the Alfvén speed with the wave period of the initial photospheric velocity driver.

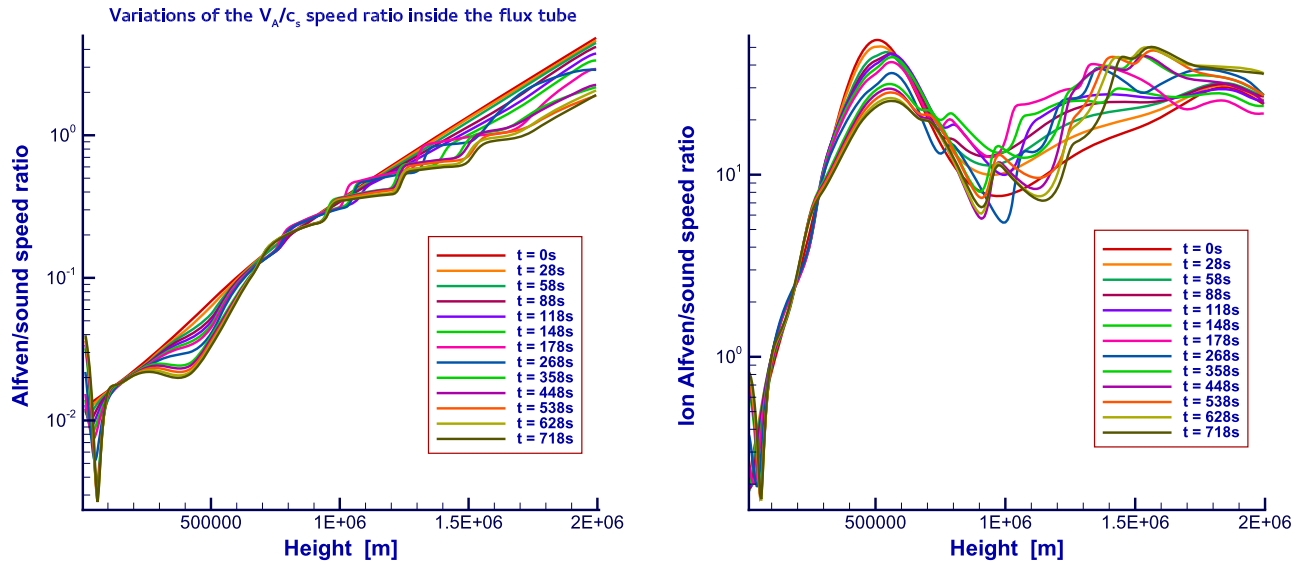

Figure 8. Altitudinal variation of the total Alfvén to sound speed ratio in the center of the magnetic flux tube and its temporal variation with the wave period of the initial driver.

neutrals are not directly affected by the magnetic field and therefore they should not enter in the calculation of the Alfvén speed. On the other hand, the high collisional rate between ions and neutrals forces the two species to move together and within an MHD picture only the total mass density plays a role. If we look at the V_A/c_s ratio, when the Alfvén speed is calculated based on the total density, the plasma β remains high in the entire photosphere and above until approximately 1.7 Mm in the upper chromosphere, where β becomes on the order of unity. In the uppermost chromosphere, $\beta < 1$, therefore in this region the magnetic field plays a role and the plasma is no longer governed by hydrodynamics.

The ratio of Alfvén to sound speed on the left panel is very low close to the solar surface and increases with heliocentric distance. At the bottom of the chromosphere in the center of the magnetic flux tube the Alfvén speed is approximately two orders of magnitude slower than the sound speed. At 1 Mm it varies between 0.25 and 0.28, depending on the simulation time. Due to the magnetic field diffusion, the Alfvén speed slightly decreases in time, which results in a lower V_A/c_s ratio. At 1.5 Mm the ratio increases to 0.5–0.8 and close to 1.8 Mm the two speeds match, which in MHD models marks the threshold of plasma $\beta = 1$. The highest ratio of the two speeds is reached at the top of the chromosphere and is of the order of 3.2, which would correspond to a plasma $\beta = 0.1$ in the single fluid description. We should note that in the estimates above the Alfvén speed is calculated based on the total mass density, which includes ions and neutrals. When we consider the classical Alfvén speed which was invented for fully ionized media and is based on the plasma fluid density only (ions and electrons), then the flow becomes supersonic at much lower heights, approximately above 150 km.

Figure 9 depicts the altitudinal variation of the kinetic energy density of neutrals at the longitudinal position of the

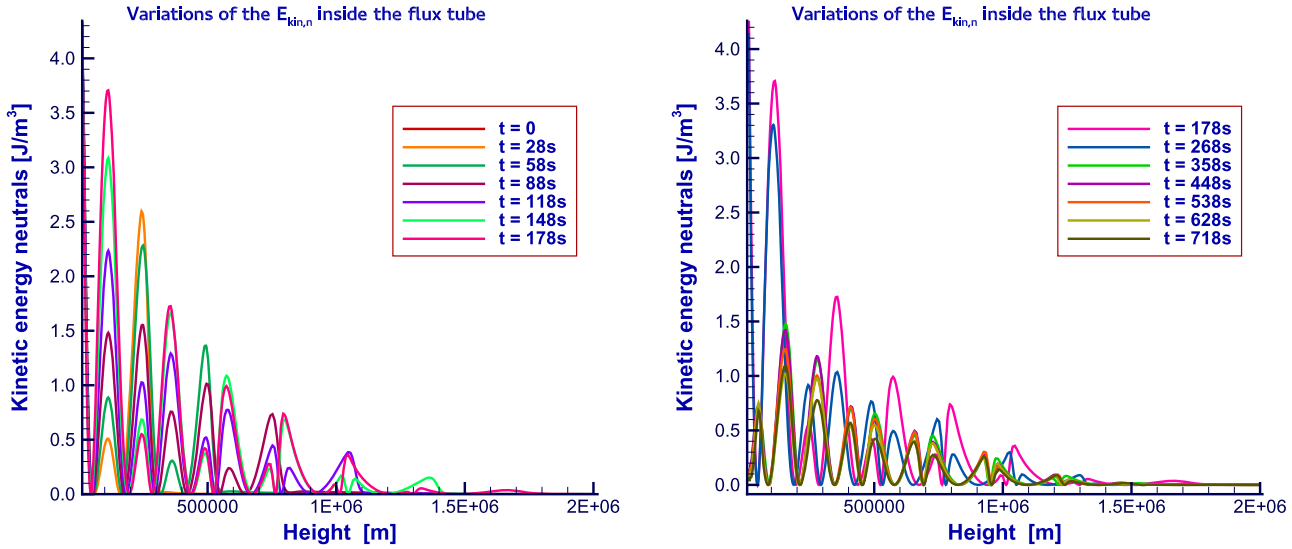

Figure 9. Altitudinal dependence of the kinetic energy of neutrals inside the magnetic flux tube as a function of the period of the initial driver. As the waves propagate phase mixing occurs and the period of the oscillations is changed.

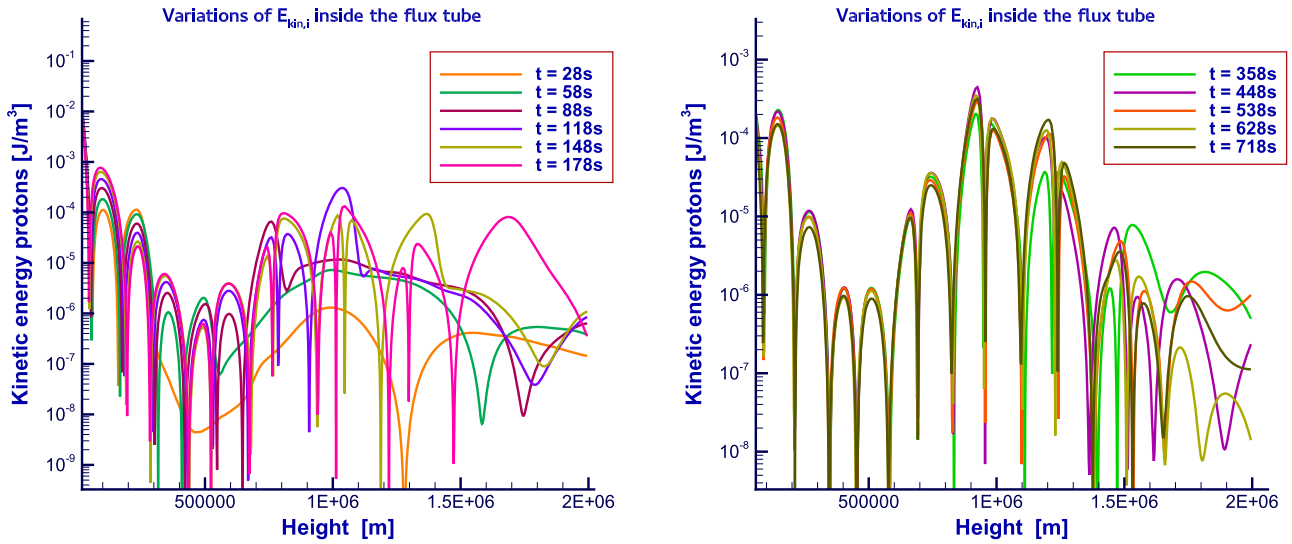

Figure 10. Altitudinal dependence of the kinetic energy of the plasma at different times. The selected time intervals are in multiples of the initial period of the imposed photospheric velocity driver.

photospheric driver as a function of the driver period. The left and the right panels represent different instances of time, which are proportional to the period of the initial driver. At $t = 0$ there are no flows in the system and the kinetic energy for both species is zero. Within the first six wave periods the kinetic energy in the photosphere and the lower chromosphere remains in phase with the period of the driver and the kinetic energy gradually decreases with distance as the neutral density gets depleted. After the waves reach the upper chromosphere and cross the $\beta = 1$ region the period of the velocity oscillations changes, which results in out-of-phase fluctuations for the kinetic energy of the neutrals.

Figure 10 shows the kinetic energy density of ions as a function of height and the period of the initial driver. On the left panel once again we can see that it takes about six periods for the waves to reach the upper chromosphere. The drop in the kinetic energy around 500 km is due to the trough in the initial density profile at this location, see Figure 1. The currents induced by the Lorentz force in the upper chromosphere cause some additional flows and different frequency velocity oscillations, which quickly become in phase with the initial driver as the driven oscillations reach the given height. The right panel shows that at a later stage (358 s approximately correspond to 12 periods of the initial driver), the ion kinetic energy fluctuations are fully in phase in the lower and middle chromosphere and, similar to the sound speed, their period changes in the upper chromosphere above 1.7 Mm where the plasma β becomes on the order of unity and below.

3.2.3. Wave-induced Loss of Ionization-recombination Equilibrium

Another aspect of the applied velocity driver is the effect of the induced oscillations on the chemical reactions in the system. Figures 11 and 12 show 2D contour plots with the change of the ionization and the recombination rates induced by the initial driver. The ionization becomes affected by the waves more quickly than the recombination, which results in local loss of chemical equilibrium.

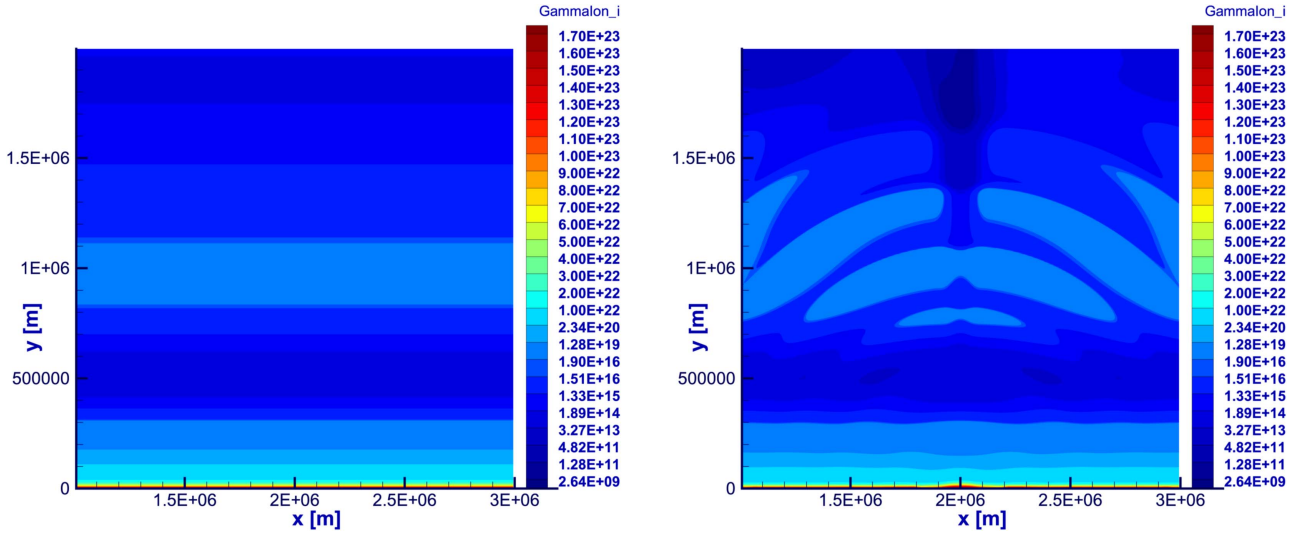

Figure 11. Evolution of the plasma ionization rate. The left panel represents the initial reaction rate, whereas the right one shows the ionization rate at $t = 458$ s.

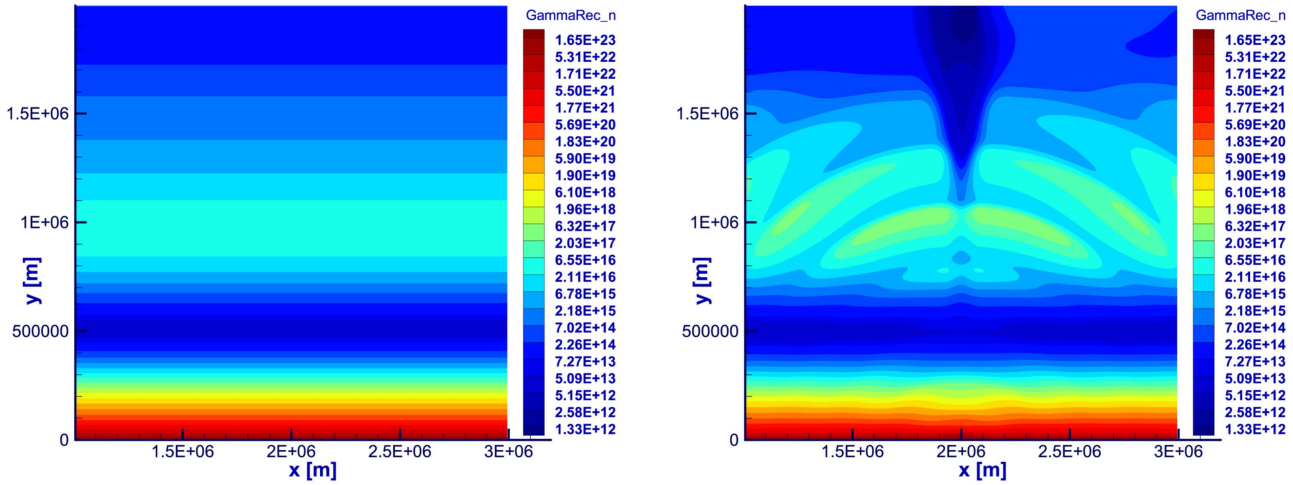

Figure 12. Evolution of the plasma recombination rate. The left panel represents the initial reaction rate, whereas the right one shows the ionization rate at $t = 458$ s.

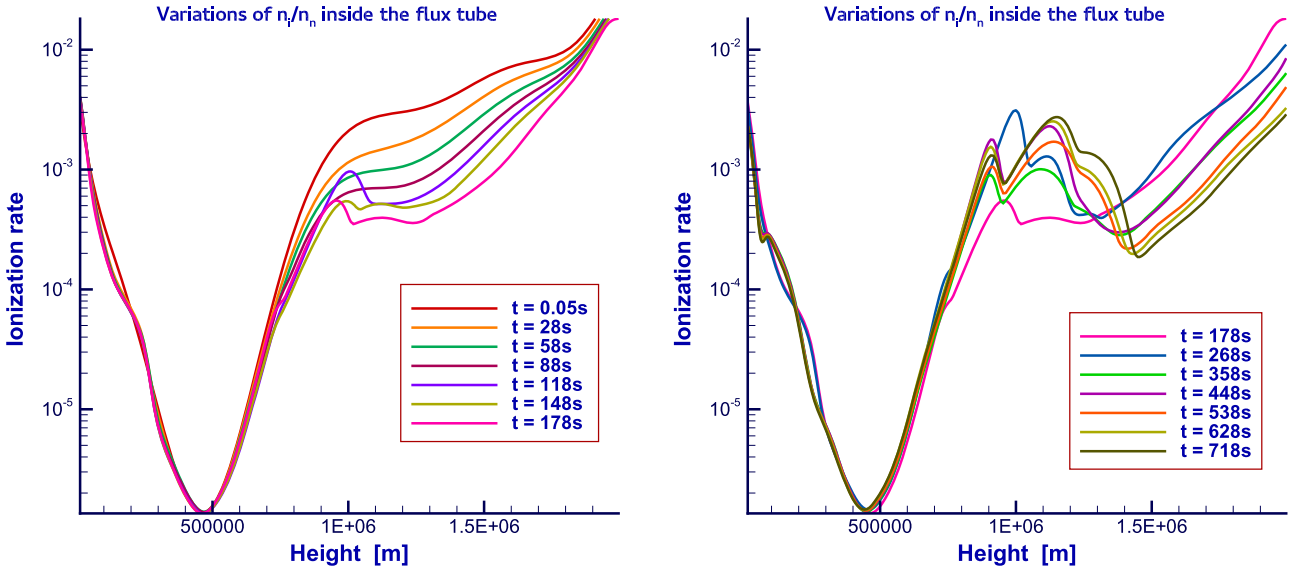

Figure 13. Changes in the ionization fraction n_i/n_n as a function of time for similar intervals as shown on Figure 10.

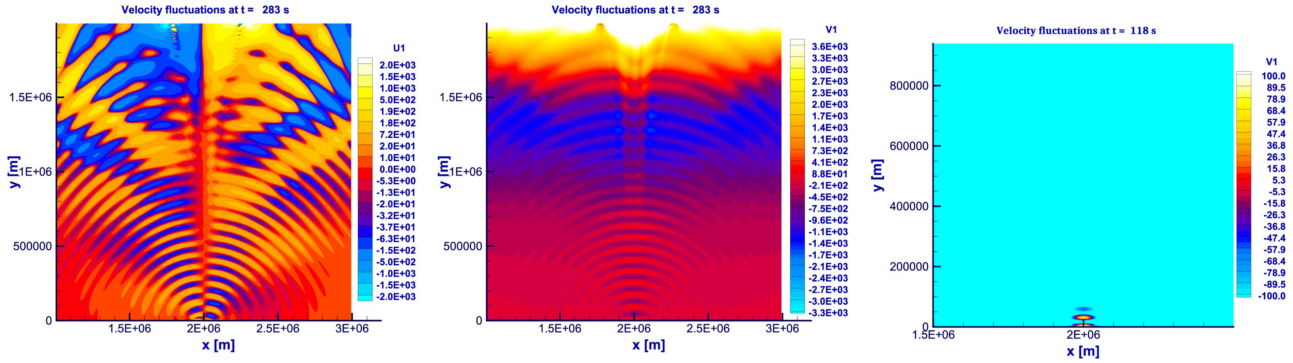

Figure 14. Horizontal (left) and vertical (middle) velocity fluctuations excited by initial photospheric velocity driver with a 10 s period. The driver excites high-frequency fast and slow magnetoacoustic waves, which propagate throughout the chromosphere and are subject to beating and modulation. The right panel shows the pressure pulses excited by a high-frequency driver with a period of 3 s.

Finally, Figure 13 shows the change of ionization fraction n_i/n_n caused by the initial driver inside the magnetic flux tube. Due to the several orders of magnitude difference between the number density of ions and neutrals in the photosphere and the lower chromosphere, the ionization fraction there remains almost unchanged by the driven oscillations. For heights $\geqslant$1 Mm, where the ion mass density reaches a local maximum, we observe the onset of related fluctuations in the ionization rate. The period of the oscillations changes in time and the relative number density of ions decreases in time in the upper chromosphere above 1.7 Mm, where the loss of chemical equilibrium results in recombination rate prevailing over the ionization.

The same results are observed for the cases of higher and lower frequency drivers, as the ionization and recombination rates are naturally affected by the excited compressible fluctuations, such as the fast magnetosonic waves.

3.3. Effects of the Driver Period

To study the effect of the photospheric velocity driver at the lower boundary on the excited plasma fluctuations we have considered several cases with different driven wave frequencies. In the subsection above, we applied a driver with a period of 30 s, which represents the conditions previously studied by MHD modeling of the chromosphere in Fedun et al. (2011). In this subsection, we gradually decrease the period of the initial velocity driver and present the resulting wave propagation for a vertical photospheric velocity drivers with periods of 10 and 3 s and corresponding angular frequencies of $\omega = 0.6$ Hz and $\omega = 2.1$ Hz. Figure 14 shows the corresponding plasma velocities for these two higher frequency drivers. The left and the middle panels illustrate the vertical and horizontal velocity components for the driver's period of 10 s, whereas the right panel shows the vertical velocity for the case of 3 s. In the case of $\omega = 0.6$ Hz, the horizontal and vertical velocity components show different patterns, suggesting different speeds for the excited slow and fast magnetosonic fluctuations. The plots also suggest the presence of beating and of some modulation of the initially excited wave fronts.

In the case of a much faster driver with a period of 3 s (corresponding frequency of approximately 2.1 Hz), the excited fluctuations seem to be predominantly field-aligned pressure pulses, which do not propagate throughout the entire chromosphere, but affect localized areas along the flux tube close to the photosphere. The effect of different drivers on the properties of Alfvén waves and the modification of the velocity of magnetosonic waves in the presence of neutrals have been previously studied within a multi-fluid approach by Soler et al. (2013a 2013b). Figure 14 suggests that these high-frequency oscillations do not generate large-amplitude fast waves and that their strength is insufficient to overcome the prevailing downflows in the photosphere caused by the unstable atmosphere due to the slight ion pressure imbalances. The velocity of the excited pulsations approximately corresponds to the expected speed of the slow magnetoacoustic waves for the given plasma conditions at the photosphere. Although constantly driven, within 250 s the high-frequency waves are fully submerged in the photospheric downflows. Furthermore, due to the density profile, the slow wave speed is expected to increase with height, nevertheless, the driven high-frequency waves in our model do not reach further than 150 km heights and are damped and/or suppressed higher in the photosphere.

We note that in the case of a horizontal velocity driver we do not observe the generation of fast magnetosonic waves, but rather the generation of Alfvén-like slow waves moving with the local Alfvén speed. Due to the dominant density of the neutrals and the selected weak photospheric magnetic field, the effective Alfvén speed is very slow (120 m s^{-1}) and the waves take a very long time to propagate. Similar to the slow magnetoacoustic modes, the Alfvén waves are further suppressed by the unstable chromospheric downflows.

4. Summary and Concluding Remarks

Within the fully 3D CoolFluid framework we used a two-fluid numerical simulation setup, which treated the charged particles within a generalized MHD approximation and considered a separate fluid of neutrals. The two fluids are coupled through collisions and chemical reactions, such as impact ionization and radiative recombination. The newly developed simulation module includes the effects of a gravitational force imposed on the initial stratified density and temperature profiles, given by a modified VAL C chromospheric model. Our simulations take into account Braginskii collisional transport coefficients with anisotropic heat conduction, *Spitzer*-type resistivity, and accounts for the basic chemical reactions in a hydrogen plasma. We initialized the simulations with a simple Gaussian magnetic flux tube, which diffuses in time and opens, starting to form a magnetic funnel. To compare this to existing MHD and generalized MHD models we imposed initial thermal and chemical equilibrium.

We included a photospheric velocity driver at the footpoint of the magnetic field and followed the evolution of the system in the presence of the driven sound and fast magnetosonic waves. Within five minutes of simulated real time, the initial driver with a 30 s period induces a loss of chemical equilibrium with a dominant recombination in the upper chromosphere and gradual reduction of the ionization fraction in time. This process occurs even faster in the case of the higher frequency driver. Regardless of the selected low magnitude of the magnetic field, we find significant heating of the higher chromospheric layers outside the magnetic flux tube with some overall cooling at low to mid-low altitudes. Significant cooling is also observed in the upper chromospheric layers inside the flux tube, where the temperature can be more than 2000 K degrees cooler than the surrounding plasma outside the flux tube. This cooling is partially counterbalanced by the heating due to the slightly unstable convecting atmosphere. The plasma heating observed at the wave fronts of the propagating fast magnetosonic fluctuations driven by the initial velocity driver as well as the heating outside the magnetic flux tube in the upper chromosphere account for a temperature increase of 500 K up to 1000 K. The observed heating strongly depends on the initial driver: the vertical velocity driver heats the chromospheric plasma more than the horizontal one. The horizontal velocity driver at the selected frequency, in our case, does not excite fast waves and does not lead to significant heating. Furthermore, the Alfvénic slow waves excited by the horizontal driver travel extremely slowly in the photosphere (with less than $120\,\mathrm{m\,s^{-1}}$) and do not propagate in the chromosphere within the simulation times considered here. This comparison between the vertical and horizontal drivers significantly differs from the results of previous single fluid MHD studies of chromospheric wave propagation, where slow magnetosonic waves were excited by the horizontal velocity driver (Khomenko & Collados 2006, Khomenko et al. 2008, Fedun et al. 2011). With both drivers we observed depletion of the number densities of ions and neutrals in the upper region of the magnetic flux tube, where the Lorentz force becomes important as the plasma β and V_A/c_s ratio increase. As the Alfvén speed becomes faster than the sound speed in the case of the vertical velocity driver, we observe a mode conversion with a transformation from fast to slow magnetosonic waves. This conversion appears particularly strong for the case of a higher frequency velocity driver.

Within our model most of the net plasma heating outside the flux tube in the upper chromosphere is wave-based and is related to kinetic to thermal energy conversion as the wave fronts of the fast magnetosonic waves steepen. In the current plasma-neutral interactions we do not observe strong heating along the perpendicular component of the current, as expected from MHD models with partial ionization effect relying on Ambipolar diffusion terms Khomenko & Collados (2012), Soler et al. (2015), Martínez-Sykora et al. (2015). Within the current multi-fluid approach the plasma heating due to the partial ionization effects, if present, is either more isotropic and not bound to the direction perpendicular to the external magnetic field profile, or it is fully overcome by the dominant wave-based heating. We should note that the partial ionization effects in our study are not very strong and the main energy source for heating are the excited magnetosonic fluctuations. The role of the partial ionization could perhaps become more prominent for stronger magnetic fields. Although this paper does not discuss in details the redistribution of the different energy types and the conversion from kinetic to thermal energy, we have to mention that there is energy transport from the photosphere throughout the chromosphere. Apart from kinetic energy transported through the chromosphere in the form of waves, there is also an associated electromagnetic energy transfer. The estimated Poynting flux related to the fast magnetosonic waves is much stronger in the horizontal than in vertical direction. However, we expect that to change whenever slow magnetosonic or Alfvén waves are excited in the system, as already suggested by some preliminary model results. To further improve our model and make it better suitable for longer wave propagation studies we would consider implementing additional wave damping layer, similar to what had been proposed and implemented for MHD simulations by (Khomenko et al. 2008).

This work was supported by project grant C 90347 (ESA Prodex 9) and FWO 12K1416N postdoctoral fellowship at CmPA, KU Leuven. This work was partially co-funded by projects GOA/2015-014 (KU Leuven) and G.0A23.16N (FWO-Vlaanderen). This research has been funded by the Interuniversity Attraction Poles Programme initiated by the Belgian Science Policy Office (IAP P7/08 CHARM). The computational resources and services used in this work were provided by the VSC (Flemish Supercomputer Center), funded by the Research Foundation - Flanders (FWO) and the Flemish Government - department EWI. A.A.L. is grateful to the IWT PhD fellowship for the support during this research.

References

Alvarez Laguna, A., Lani, A., Deconinck, H., Mansour, N. N., & Poedts, S. 2016, JCoPh, 318, 252
Avrett, E. H., & Loeser, R. 2008, ApJS, 175, 229
Balay, S., Abhyankar, S., Adams, M. F., et al. 2015, PETSc, Web page, http://www.mcs.anl.gov/petsc
Braginskii, S. I. 1965, RvPP, 1, 205
Carlsson, M., Hansteen, V. H., Gudiksen, B. V., Leenaarts, J., & de Pontieu, B. 2016, A&A, 585, A4
Cheung, M. C. M., & Cameron, R. H. 2012, ApJ, 750, 6
Cox, D. P., & Tucker, W. H. 1969, ApJ, 157, 1157
De Pontieu, B., Rouppe van der Voort, L., McIntosh, S. W., et al. 2014, Sci, 346, 1255732
Degrez, G., Lani, A., Panesi, M., Chazot, O., & Deconinck, H. 2009, JPhD, 42, 194004
Fedun, V., Erdélyi, R., & Shelyag, S. 2009, SoPh, 258, 219
Fedun, V., Shelyag, S., & Erdélyi, R. 2011, ApJ, 727, 17
Fontenla, J. M., Avrett, E. H., & Loeser, R. 1993, ApJ, 406, 319
Garicano Mena, J., Pepe, R., Lani, A., & Deconinck, H. 2015, CCoPh, 17, 682
Gent, F. A., Fedun, V., Mumford, S. J., & Erdélyi, R. 2013, MNRAS, 435, 689
Gudiksen, B. V., Carlsson, M., Hansteen, V. H., et al. 2011, A&A, 531, A154
Hansteen, V. H., Carlsson, M., & Gudiksen, B. 2007, in ASP Conf. Ser. 368, The Physics of Chromospheric Plasmas, ed. P. Heinzel, I. Dorotovič, & R. J. Rutten (San Francisco, CA: ASP), 107
Hansteen, V. H., De Pontieu, B., Rouppe van der Voort, L., van Noort, M., & Carlsson, M. 2006, ApJL, 647, L73
Khomenko, E., & Collados, M. 2006, ApJ, 653, 739
Khomenko, E., & Collados, M. 2012, ApJ, 747, 87
Khomenko, E., Collados, M., & Felipe, T. 2008, SoPh, 251, 589
Khomenko, E., Díaz, A., de Vicente, A., Collados, M., & Luna, M. 2014, A&A, 565, A45
Knight, D., Longo, J., Drikakis, D., et al. 2012, PrAeS, 48–49, 8
Lani, A., Panesi, M., & Deconinck, H. 2013a, CCoPh, 13, 479
Lani, A., Yalim, M. S., & Poedts, S. 2014, CoPhC, 185, 2538
Leake, J. E., Lukin, V. S., & Linton, M. G. 2013, Magnetic Reconnection in a Weakly Ionized Plasma, arXiv:1302.3287
Leake, J. E., Lukin, V. S., Linton, M. G., & Meier, E. T. 2012, ApJ, 760, 109
Martínez-Sykora, J., De Pontieu, B., & Hansteen, V. 2012, ApJ, 753, 161

Martínez-Sykora, J., De Pontieu, B., Hansteen, V., & Carlsson, M. 2015, RSPTA, 373, 20140268
Martínez-Sykora, J., De Pontieu, B., Hansteen, V. H., & Gudiksen, B. 2016, ApJ, 817, 46
Martínez-Sykora, J., Hansteen, V., De Pontieu, B., & Carlsson, M. 2009, ApJ, 701, 1569
Meier, E. T., & Shumlak, U. 2012, PhPl, 19, 072508
Moore, R. L., & Fung, P. C. W. 1972, SoPh, 23, 78
Munafo, A., Lani, A., Bultel, A., & Panesi, M. 2013, PhPl, 20, 073501
Munz, C.-D., Ommes, P., & Schneider, R. 2000, CoPhC, 130, 83
Panesi, M., & Lani, A. 2013, PhFl, 25, 057101
Panesi, M., Lani, A., Magin, T., et al. 2007, in 38th AIAA Plasmadynamics and Lasers Conf., Numerical Investigation of the non Equilibrium Shock-layer Around the Expert Vehicle, AIAA Paper 2007-4317
Pereira, T. M. D., Carlsson, M., De Pontieu, B., & Hansteen, V. 2015, ApJ, 806, 14
Santos, P. D., & Lani, A. 2016, CoPhC, 202, 233
Shelyag, S., Khomenko, E., de Vicente, A., & Przybylski, D. 2016, ApJL, 819, L11
Smirnov, B. M. 2003, Physics of Atoms and Ions (New York: Springer-Verlag)
Soler, R., Ballester, J. L., & Zaqarashvili, T. V. 2015, A&A, 573, A79
Soler, R., Carbonell, M., & Ballester, J. L. 2013a, ApJS, 209, 16
Soler, R., Carbonell, M., Ballester, J. L., & Terradas, J. 2013b, ApJ, 767, 171
Spitzer, L. 1956, Physics of Fully Ionized Gases (New York: Interscience)
Vernazza, J. E., Avrett, E. H., & Loeser, R. 1981, ApJS, 45, 635
Voronov, G. S. 1997, ADNDT, 65, 1
Vranjes, J. 2014, MNRAS, 445, 1614
Vranjes, J., & Krstic, P. S. 2013, A&A, 554, A22
Yalim, M. S., Vanden Abeele, D., Lani, A., Quintino, T., & Deconinck, H. 2011, JCP, 230, 6136
Zhang, W., Lani, A., & Panesi, M. 2016, PoP, 23, 073512